

Electronic structure and carrier dynamics of the ferromagnetic semiconductor $\text{Ga}_{1-x}\text{Mn}_x\text{As}$

E. J. Singley* and K. S. Burch

*Department of Physics, University of California, San Diego, California 92093-0354, USA*R. Kawakami,[†] J. Stephens, and D. D. Awschalom*Department of Physics, University of California, Santa Barbara, California 93106, USA*

D. N. Basov

Department of Physics, University of California, San Diego, California 92093-0319, USA

(Received 8 November 2002; revised manuscript received 30 April 2003; published 21 October 2003)

Infrared spectroscopy is used to study the doping and temperature dependence of the intragap absorption in the ferromagnetic semiconductor $\text{Ga}_{1-x}\text{Mn}_x\text{As}$, from a paramagnetic, $x=0.017$ sample to a heavily doped, $x=0.079$ sample. Transmission and reflectance measurements coupled with a Kramers-Kronig analysis allow us to determine the optical constants of the thin films. All ferromagnetic samples show a broad absorption resonance near 200 meV, within the GaAs band gap. We present a critical analysis of possible origins of this feature, including a Mn-induced impurity band and intervalence band transitions. The overall magnitude of the real part of the frequency dependent conductivity grows with increasing Mn doping, and reaches a maximum in the $x=0.052$ sample where T_C saturates at the highest value (~ 70 K) for the series. We observe spectroscopic signatures of compensation and track its impact on the electronic and magnetic state across the Mn phase diagram. The temperature dependence of the far infrared spectrum reveals a significant decrease in the effective mass of itinerant carriers in the ferromagnetic state. A simple scaling relation between changes in the mass and the sample magnetization suggest that the itinerant carriers play a key role in producing the ferromagnetism in this system.

DOI: 10.1103/PhysRevB.68.165204

PACS number(s): 75.50.Pp, 71.55.Eq, 78.20.-e

I. INTRODUCTION

The discovery of ferromagnetic order induced by doping common III-V semiconductors has recently generated a great deal of interest.¹ With transition temperatures in excess of 100 K these systems are emerging as one of the most promising materials base for spin electronics applications.² Low temperature epitaxial growth techniques have allowed for the incorporation of large amounts of Mn atoms, beyond the bulk solubility limit, in both InAs and GaAs. In GaAs, up to 8% of the Ga atoms may be replaced by Mn. The Mn atom generally sits in place of a Ga atom providing a local magnetic moment, and acts as an acceptor, thus doping a hole into the system. These high dopings also inevitably introduce disorder in the form of Mn interstitials which are believed to act as double donors. A natural explanation for the resultant magnetic order is in terms of the itinerant doped holes mediating the ferromagnetism of the localized Mn spins.³

A more comprehensive picture of the ferromagnetic state requires knowledge of the Mn induced changes in the GaAs electronic structure at high doping levels. Optical absorption measurements on nonmagnetic GaAs doped with Mn in the very dilute limit indicate that Mn forms a shallow acceptor level at 110 meV above the valence band.^{4,5} However, the concept of an isolated impurity level is likely to break down at high doping levels (few atomic percent) needed to initiate the ferromagnetic state in $\text{Ga}_{1-x}\text{Mn}_x\text{As}$. Indeed, most band structure calculations predict a substantial hybridization of the GaAs bands with Mn d levels in this doping regime.⁶⁻¹³ Experimental verification of this proposal is found in the results of core-level photoemission experiments which indi-

cate a strong As $4p$ Mn $3d$ hybridization.¹⁴ Direct measurements of the electronic states in $\text{Ga}_{1-x}\text{Mn}_x\text{As}$ from angle resolved photoemission spectroscopy (ARPES) show Mn-induced states both 3–4 eV below the top of the valence band, and also very near the Fermi energy (E_F).^{15,16} The low energy band has small but finite spectral weight at E_F with little dispersion, and is spread out in energy by nearly 1 eV. These Mn-induced states at E_F are a critical component for carrier mediated ferromagnetism in the III-V series. Unfortunately, the present resolution (100 meV) of the ARPES experiments precludes a detailed inspection of these states near E_F . Recent tunneling measurements have shown E_F shifting from midgap to the top of the valence band with increased doping.¹⁷ These studies find a significant broadening of the valence band, suggestive of hybridization with a Mn-induced impurity band. Currently little is known about the dynamical properties of conducting holes since the vast majority of experimental studies of $\text{Ga}_{1-x}\text{Mn}_x\text{As}$ are focused on transport measurements in the dc limit.

Infrared spectroscopy offers a unique perspective on the electronic structure and charge dynamics of solids by providing experimental access to the critical energy range extending from a few meV to several eV. The high resolution (<1 meV) enables a detailed examination of fine features near E_F . Previous measurements of the absorption coefficient on thin films of $\text{Ga}_{1-x}\text{Mn}_x\text{As}$ have detected a resonance near 200 meV.^{18,19} While its origin is as yet unresolved, this feature has been attributed to a small polaron,¹⁸ impurity band absorption,¹⁸⁻²¹ and intervalence band transitions.^{19,22-24} Additionally these experiments have found a strong growth of the far-infrared spectral weight below T_C .

A comprehensive analysis of the information obtained through spectroscopic experiments is hardly possible without extracting the *optical constants* of the studied material from measured transmission and/or reflectance spectra. Indeed, the dissipative part of the optical constants [the real part of the complex conductivity $\sigma_1(\omega)$ or imaginary part of the dielectric function $\epsilon_2(\omega)$] uncovers resonances attributable to different excitation channels in a system. Moreover, a variety of sum rules that can be formulated for the optical constants permit extraction of quantitative information from the data pertinent, for example, to the determination of the effective masses and/or carrier densities.²⁵ Since sum rules can be traced back to fundamental conservation laws, this analysis offers opportunities to infer a wealth of information in a model-independent way. Recently we have published our initial results of a study of the optical conductivity of ferromagnetic Ga_{1-x}Mn_xAs films.²⁶ Here we report on the detailed doping and temperature dependence of the infrared properties of a series of Ga_{1-x}Mn_xAs films throughout the Mn-doping phase diagram. An examination of doping trends allows us to distinguish between two types of compensating defects: As_{Ga} antisites and Mn_i interstitials which play a pivotal role in defining both the electronic and magnetic state of the Ga_{1-x}Mn_xAs system.²⁷⁻²⁹ We confirm the existence of the 200 meV resonance in the intragap conductivity of Ga_{1-x}Mn_xAs. We show that this feature is specific to the response of ferromagnetic samples. Applying a sum rule analysis to our data we found that charge carriers in ferromagnetic films reveal significant enhancement of their effective mass compared to the valence band mass. Below the Curie temperature we observe a strong increase of the low-energy spectral weight consistent with the lowering of m^* values that tracks the temperature dependence of magnetization. We discuss these results in the context of recent proposals for the electronic structure of ferromagnetic III-V compounds.

This paper is organized in the following manner. In Sec. II we briefly outline the experimental procedures. Also included is an appendix (Sec. VI) with a detailed discussion of a novel method of extracting the optical constants of the Ga_{1-x}Mn_xAs films from a combination of transmission and reflectance measurements, supplemented with a Kramers-Kronig analysis of the transmission data. In Sec. III we present both the doping and temperature dependence of $\sigma_1(\omega)$ for the Ga_{1-x}Mn_xAs films. Section IV A discusses the effects of compensation in these heavily doped systems. In Sec. IV B we infer the gross features of the electronic structure of Ga_{1-x}Mn_xAs from the conductivity data and discuss the evolution of the electronic structure with Mn doping. The temperature dependence of the conductivity in the ferromagnetic state is analyzed in terms of an effective mass change in Sec. IV C. Finally we summarize our findings and provide an outlook on future experiments in Sec. V.

II. EXPERIMENTAL PROCEDURES

Thin films of Ga_{1-x}Mn_xAs were grown with the low temperature molecular-beam epitaxy method.¹ The films had a thickness of 0.5 μm , and were grown on single crystal GaAs substrates 0.5 mm thick. Table I shows the different Mn con-

TABLE I. Magnetic and electronic parameters of Ga_{1-x}Mn_xAs thin films. Ferromagnetic transition temperature, T_C , Magnetization at 5 K, M , and effective mass values, m^* , are determined as described in the text.

x	0.000	0.017	0.028	0.040	0.052	0.066	0.079
T_C (K)	<5	<5	30	45	70	70	70
M (emu/cm ³)	0	0	13	23	26	32	28
m_{min}^* (m_e)			0.8	0.8	0.7	0.9	1.2
m_{max}^* (m_e)			24	19	15	20	26

centrations used, and summarizes some of the magnetic and electronic properties. The $x=0.017$ sample is paramagnetic down to the lowest measured temperatures (5 K); all other Mn-doped samples showed a well defined ferromagnetic transition. In addition, we examined the infrared response of a 0.5 μm film of GaAs prepared using the low-temperature growth at $T=260^\circ\text{C}$ which is an optimized condition for epitaxy of ferromagnetic films.

Infrared transmission experiments were performed between 292 K and 5 K, well above and below the ferromagnetic transition temperatures of the samples. The energy range covered in the experiment extends from 15 cm^{-1} to 12 000 cm^{-1} (the band gap in GaAs). The ratio of the transmission through the film and substrate to the transmission of a blank substrate was measured. A novel approximation free method^{30,31} described in the Appendix was used to calculate an effective single-layer transmission (T_{KK}) of the Ga_{1-x}Mn_xAs films. A Kramers-Kronig analysis of T_{KK} yields the accompanying phase change, Θ . A combination of T_{KK} and Θ allows all of the complex optical constants of the Ga_{1-x}Mn_xAs film, such as the optical conductivity, $\sigma(\omega)$, to be calculated. To eliminate uncertainties related to the Kramers-Kronig (KK) analysis of the transmission, we have also measured the reflectance of the films for $\omega > 3000 \text{ cm}^{-1}$ at 292 K. With the raw transmission and reflectance data the optical constants can be calculated directly, which serves to set a constraint on the KK generated phase.

III. RESULTS AND ANALYSIS

The measured transmission spectra, which is the ratio between the transmission through both the Ga_{1-x}Mn_xAs film and substrate, and the bare substrate ($T_{meas} = T_{2l}/T_s$) is plotted in Fig. 1 for all studied samples at $T=292 \text{ K}$ and 5 K .³² For the $x=0$ film [low-temperature (LT) GaAs] we find that T_{meas} is indistinguishable from that of bulk GaAs substrate for $\omega < 7000 \text{ cm}^{-1}$. At higher frequencies we observe a substantial drop of T_{meas} which is especially prominent as the band gap of GaAs is approached. For the $x=0.017$ sample, the T_{meas} spectra are similar to the LT GaAs data. However, the transmission drop close to the gap edge is stronger and the onset of this feature starts at a lower frequencies. A qualitative change in the transmission data occurs between $x=0.017$ and $x=0.028$, coincident with the onset of ferromagnetism in our series of films. Here T_{meas} is substantially suppressed below 1, even at low frequencies. Additionally, a new feature emerges in all of these samples. Near

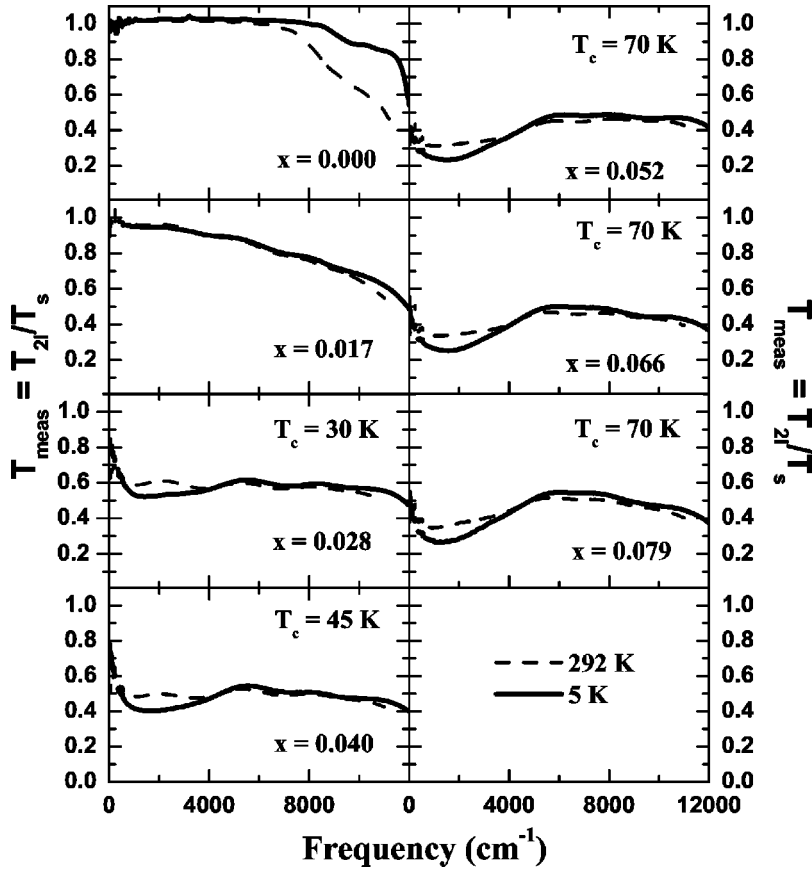


FIG. 1. The measured transmission which is the two layer transmission normalized to the transmission of a blank substrate ($T_{meas} = T_{2l}/T_s$) is shown for all seven samples at $T = 292$ K and 5 K. Deviations from $T_{meas} = 1$ is an indication of absorption in the $\text{Ga}_{1-x}\text{Mn}_x\text{As}$ film. As the Mn doping is increased the overall level of T_{meas} decreases. Additionally, a strongly temperature dependent minimum is observed near 2000 cm^{-1} for all ferromagnetic samples. The weak oscillations observed throughout the frequency range in all samples is due to interference within the film.

2000 cm^{-1} a minimum is observed, clearly seen at low temperatures for the films with low doping, and at all temperatures for the higher Mn concentration samples. This minimum near 2000 cm^{-1} should be distinguished from the weak periodic oscillations observed throughout the spectra. The latter weak structure in $T(\omega)$ can be attributed to interference within the $\text{Ga}_{1-x}\text{Mn}_x\text{As}$ film. The minimum at finite ω observed in the raw data is a clear signature of the peak in the KK generated $\sigma_1(\omega)$ discussed below.

Before discussing the full doping dependence of $\sigma_1(\omega)$, we show in Fig. 2 the paramagnetic sample with $x=0.017$, and a ferromagnetic sample ($x=0.052$) with a T_C near the maximum for the series. Also plotted is $\sigma_1(\omega)$ for undoped GaAs (Ref. 33) along with the data for the Mn free LT GaAs sample.³⁴ The spectrum of single crystal GaAs (gray line) shows the canonical features of a direct gap semiconductor: $\sigma_1(\omega)=0$, except for the sharp absorption in the far infrared ($\omega=265 \text{ cm}^{-1}$) due to a well known optically active phonon, and the sudden onset of $\sigma_1(\omega)$ signaling absorption across the GaAs band gap. These two features impose opaque regions on the energy window of our experiments, since nearly all of the light which is transmitted through the thin $\text{Ga}_{1-x}\text{Mn}_x\text{As}$ films is absorbed in the thick (0.5 mm) GaAs substrate. The changes in $\sigma_1(\omega)$ when the doping level is at 1.7% Mn (paramagnetic sample, dashed line) are relatively weak. Below 2500 cm^{-1} , $\sigma_1(\omega)$ is flat and featureless with a value of $\sim 5 \Omega^{-1} \text{ cm}^{-1}$, close to the noise floor of the current experimental setup. The most significant change is the strong broadening of the gap edge, which is

noticeable in all samples prepared using low-temperature growth. Such broadening, also observed in LT GaAs, in part can be attributed to disorder associated with As_{Ga} antisite defects.^{35,36} This structure will be discussed in the next section in the context of compensation effects in $\text{Ga}_{1-x}\text{Mn}_x\text{As}$.

Turning now to the ferromagnetic sample with $x=0.052$ (thick black line), we see a qualitative change in the spectrum. There is a strong increase in the absolute value of $\sigma_1(\omega)$ at all ω . In particular, $\sigma_1(\omega \rightarrow 0)$ has increased by nearly two orders of magnitude from the paramagnetic sample, signaling a crossover to metallic transport. The other new feature which dominates the conductivity spectrum of ferromagnetic $\text{Ga}_{1-x}\text{Mn}_x\text{As}$ is the strong resonance at $\omega \sim 2000 \text{ cm}^{-1}$. This feature is indicative of an interband transition within what was the GaAs band gap.

A common feature of the paramagnetic $x=0.017$ sample and all the ferromagnetic samples is the broad tail near the GaAs band gap. In order to more clearly focus on the Mn-doping dependence of the conductivity we plot $\sigma_1^m(\omega) = \sigma_1^x(\omega) - \sigma_1^{1.7\%}(\omega)$ in Fig. 3 for $T=292$ K. This subtraction has negligible effect on $\sigma_1(\omega)$ below 4000 cm^{-1} , and simply removes the high energy tail.

All the samples shown in Fig. 3 share the same features as the $x=0.052$ sample discussed above. A strong resonance is observed in the region of $1500\text{--}2000 \text{ cm}^{-1}$, and $\sigma_1(\omega \rightarrow 0)$ remains finite. The overall magnitude of the conductivity spectra increases with doping up to $x=0.052$, which is also the sample in where T_C saturates for the present series. We also observe reproducible structure in all the ferromag-

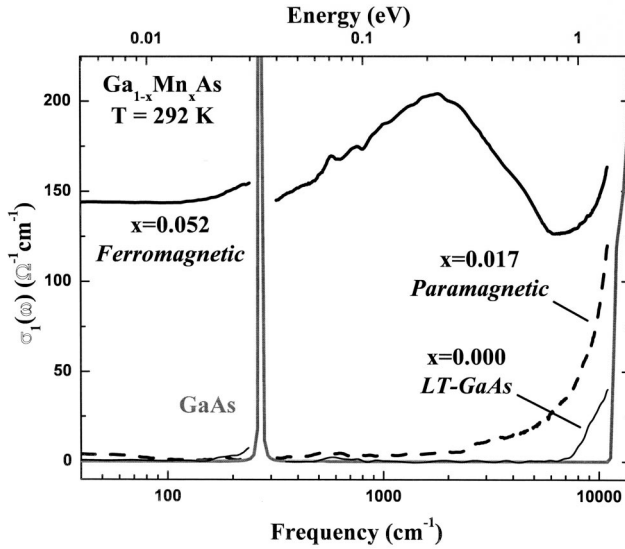


FIG. 2. Real part of the conductivity derived from measured transmission for paramagnetic $x=0.017$ sample (dashed line), ferromagnetic $x=0.052$ sample (thick solid line), and the LT GaAs film ($x=0.00$, thin black line). Also shown is the conductivity of GaAs from Ref. 33 (gray line). The conductivity of the GaAs substrate is zero except for the narrow band near 265 cm^{-1} where there is a strong phonon mode, and above $12\,000 \text{ cm}^{-1}$ where absorption across the band gap sets in. Due to the thickness of the substrate these regions are opaque to our experiment. The LT GaAs film spectrum deviates from the single crystal data above 7000 cm^{-1} where additional absorption is observed due to As_{Ga} defects. The absorption increases in this region and extends down to lower energy as 1.7% Mn is doped into the system. However, below 2500 cm^{-1} $\sigma_1(\omega)$ remains flat and featureless with a magnitude of $< 5 \text{ } \Omega^{-1} \text{ cm}^{-1}$. While the $x=0.052$ ferromagnetic sample has a similar broad band tail as at $x=0.017$, it also has qualitatively new features. Near 2000 cm^{-1} a strong interband absorption is observed. Additionally the low- ω conductivity has increased substantially.

netic samples around $7000\text{--}10\,000 \text{ cm}^{-1}$. Such an absorption in the infrared conductivity has been predicted to arise from heavy hole to split-off band transitions in the GaAs valence band.²³ In the current data set these features are only clearly visible after subtracting the conductivity spectrum of the 1.7% sample as discussed above.

The increase of the conductivity with Mn doping is a sign of increasing carrier concentration, which can be seen more clearly by calculating the effective spectral weight:

$$\frac{n}{m^*} = \frac{2}{\pi e^2} \int_0^{\Omega} \sigma_1(\omega) d\omega, \quad (1)$$

where n is the density of carriers, m^* is the effective mass, and Ω is the appropriate cutoff of the integration. The inset of Fig. 3 shows n/m^* calculated from $\sigma_1^m(\omega)$ with the integration limit of $11\,000 \text{ cm}^{-1}$, as a function of Mn concentration. The spectral weight rises strongly with Mn doping until $x=0.052$, and then decrease slowly at higher x . Non-monotonic dependence of n/m^* on the doping concentration

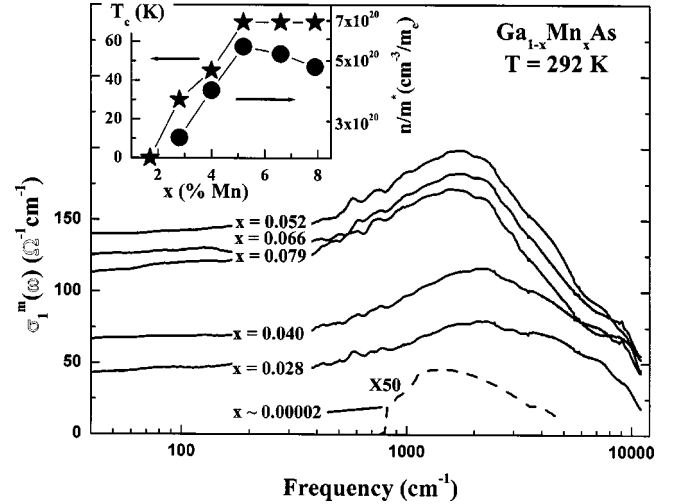


FIG. 3. In order to focus on the effects of Mn doping $\sigma_1^m(\omega) = \sigma_1^x(\omega) - \sigma_1^{x=1.7\%}(\omega)$ is plotted for all ferromagnetic samples at 5 K. All samples show an absorption feature in the midinfrared, indicative of an interband transition. As the doping increases the strength of this feature increases, along with the overall level of the $\sigma_1(\omega)$ curve. At $x=0.052$, where T_c saturates near its maximum value, $\sigma_1(\omega)$ also reaches a maximum than decreases slightly with increased doping. Also shown is $\sigma_1(\omega)$ for nonmagnetic $\text{Ga}_{1-x}\text{Mn}_x\text{As}$ (Ref. 4), in the very dilute limit with $x \sim 0.00002$. An absorption band is observed in the dilute sample starting at 800 cm^{-1} and peaked near 1500 cm^{-1} due to transitions from the valence band to the Mn-induced impurity level. There is a close correspondence between the energy scales of the absorption band in the dilute sample and ferromagnetic films. The inset shows the doping dependence of T_c and n/m^* [Eq. (1)].

is yet another indication of the presence of compensation effects that will be addressed in the next section. Also plotted in the inset is the Mn dependence of the ferromagnetic transition temperature, T_c . The correlation between carrier density and T_c , which has also been found in a number of measurements,^{37–40} argues in favor of a pivotal role of the itinerant carriers in the formation of the ferromagnetic state.

The close association between the charge response and magnetism is also found in the temperature dependence of $\sigma_1(\omega)$. The temperature dependence of the conductivity for all Mn-doped samples is displayed in Fig. 4. For the paramagnetic $x=0.017$ sample $\sigma_1(\omega)$ is shown at 292 K and 5 K. Throughout most of the spectrum there is very little T dependence. For all other samples $\sigma_1^m(\omega)$ is plotted at $T=292 \text{ K}$, T_c , and 5 K. The basic trends in the temperature dependence of all of these samples are nearly identical. Going from 292 K to T_c the finite frequency peak narrows, while the low- ω conductivity decreases. The latter trend is reversed in the ferromagnetic state and at $T < T_c$, $\sigma_1(\omega)$ increases at all $\omega < 2500 \text{ cm}^{-1}$. This leads to a nearly parallel offset between the spectra at different temperatures.

To focus more clearly on this temperature dependence, $\sigma_1(\omega)$ is shown in Fig. 5 for the $x=0.052$ sample. The top panel displays temperatures $T \geq T_c$, while the bottom panel presents the spectrum obtained at T_c along with the data at lower temperatures. A critical review of the data reveals two

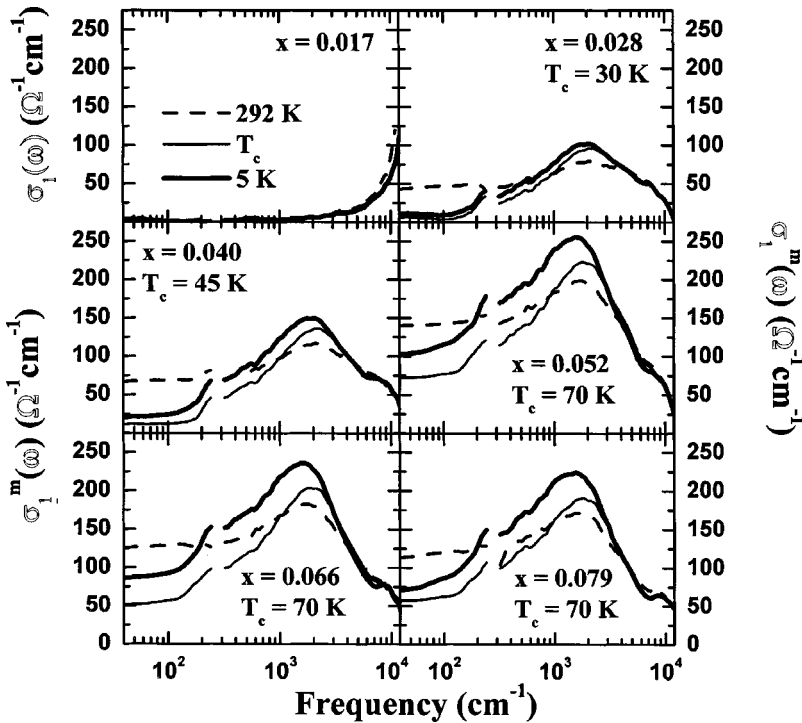


FIG. 4. Temperature dependence of the conductivity for all Mn-doped samples. For the $x = 0.017$ sample $\sigma_1(\omega)$ is plotted at $T = 292$ K and 5 K. There is only minor T dependence at high frequencies. For all other samples $\sigma_1^m(\omega) = \sigma_1^x(\omega) - \sigma_1^{x=1.7\%}(\omega)$ is shown at $T = 292$ K, T_c , and 5 K. The temperature dependence for all samples is very similar. The low frequency conductivity decreases with decreasing temperature above T_c , but increase as the temperature is lowered in the ferromagnetic state. In contrast, the peak height increases as the temperature is lowered for all T .

distinctly different behaviors in the T and ω dependence of σ_1 above and below T_c . At $T > T_c$ (top panel) strengthening of the 2000 cm^{-1} feature is accompanied by a corresponding decrease in $\sigma_1(\omega)$ below 900 cm^{-1} . As a result, the total

spectral weight remains nearly constant below $\sim 4000 \text{ cm}^{-1}$. In contrast at $T < T_c$ (bottom panel) the low- ω conductivity now increases simultaneously with the growth of the peak. This leads to an overall gain in spectral at $\omega < 4000 \text{ cm}^{-1}$. This excess spectral weight is drawn from the energy region between 4000 cm^{-1} and 8000 cm^{-1} . At even higher frequencies the spectral weight is independent of temperature.

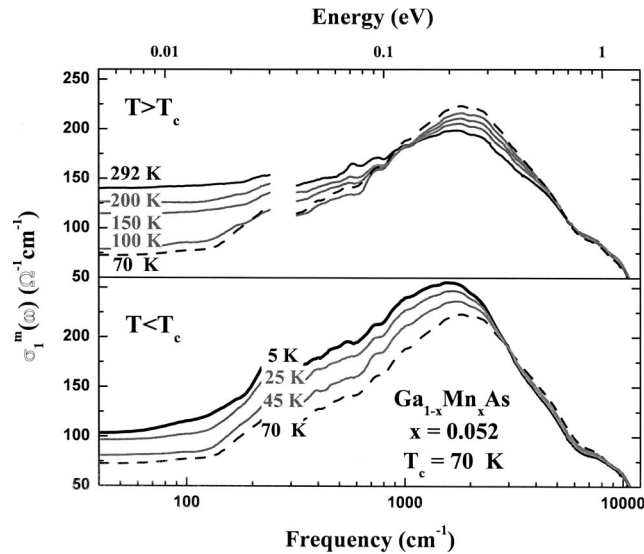


FIG. 5. Temperature dependence of $\sigma_1^m(\omega)$ for $x = 0.052$ sample on a log scale. Top panel shows $T \geq T_c$, while the bottom panel displays $T \leq T_c$. As the temperature is lowered from 292 K to T_c (top panel) the midinfrared peak narrows, shifts slightly to higher frequencies, and increases in strength. Concomitantly, there is a depression of $\sigma_1(\omega)$ below 900 cm^{-1} . Cooling below T_c in the ferromagnetic state (bottom panel) produces a qualitatively different effect. The peak now broadens and shifts to lower frequencies, but still increases in magnitude. Notably, the low- ω conductivity now increases with decreasing temperature, and there is no crossing of $\sigma_1(\omega)$ near 900 cm^{-1} at different temperatures.

The nonmonotonic temperature dependence of $\sigma_1(\omega)$, common for all ferromagnetic samples, reflects dramatic changes in the charge response at $T < T_c$. Further insights into the free carrier transport may be gained by looking at $\sigma_1(\omega)$ in the limit of $\omega \rightarrow 0$, where the response is governed entirely by intraband processes. In Fig. 6 we plot $\rho_{opt} = 1/\sigma_1(\omega = 40 \text{ cm}^{-1})$, which is an optical measure of the dc resistivity. While the magnitude of ρ_{opt} is doping dependent, all of the ferromagnetic samples share the same qualitative features of the T dependence. Below T_c the resistivity is an increasing function of temperature. Above T_c the slope of $d\rho/dT$ changes and a semiconducting character is observed in ρ_{opt} . For all ferromagnetic samples ρ_{opt} remains finite as $T \rightarrow 0$, signaling metallic transport. The slight increase in ρ_{opt} above $x = 0.052$ is likely the result of the accelerated rate of compensation at high Mn concentration. Both the temperature dependence and magnitude of ρ_{opt} is in accord with direct measurements of ρ_{dc} , for $x > 0.035$.³⁷ However, at lower doping levels dc measurements observe a negative $d\rho/dT$ over the entire temperature range, with only a shoulder visible at T_c .

The temperature dependence of $\rho(T)$ has previously been attributed to a modification of the scattering of metallic carriers by spin fluctuations below the Curie temperature.³⁷ However, this interpretation of the dc data must be reconsidered in light of the results for the dynamical conductivity

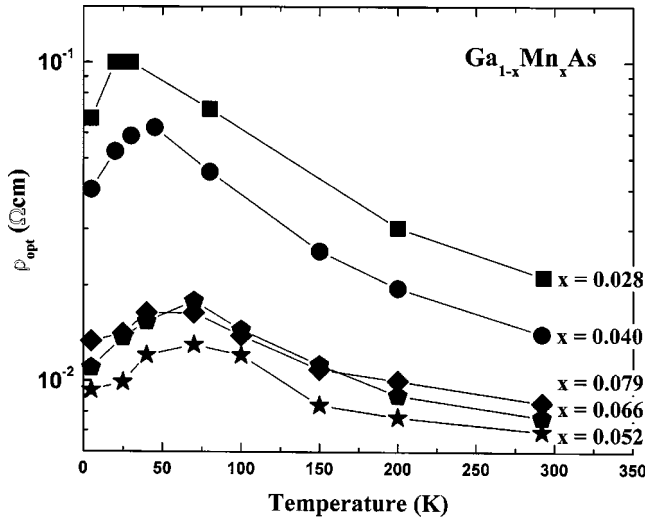


FIG. 6. Optical analog of the dc resistivity, $\rho_{opt} = 1/\sigma_1(\omega = 40 \text{ cm}^{-1})$ is plotted vs temperature for all ferromagnetic samples. The magnitude of ρ_{opt} decreases with doping until $x=0.052$, after which it saturates at a slightly higher value. All samples share the same qualitative features; below T_c , ρ_{opt} increases with increasing temperature, while in the paramagnetic state ρ_{opt} decreases. The temperature dependence of ρ_{opt} is governed by the redistribution of spectral weight as can be clearly seen in Fig. 5.

shown in Figs. 4 and 5. A strong temperature dependence in the scattering rate should lead to noticeable changes in the low- ω line shape of σ_1 as the temperature is reduced. In contrast with this expectation based on transport theories we only observe a parallel offset between the different spectra without significant modification of the frequency dependence. An alternative explanation of the dc data may be found in the strong changes in the low- ω spectral weight.^{18,26} Within the Drude theory $\rho \propto (m^*/n)(1/\tau)$, the dc resistivity is a function of both the scattering time, τ , and the itinerant carrier spectral weight, n/m^* . As suggested in Ref. 18 it appears that the nonmonotonic behavior of $\rho(T)$ is simply a further manifestation of the strong renormalization of the carrier mass at $T < T_C$.

IV. DISCUSSION

A. Spectroscopic signatures of compensation in $\text{Ga}_{1-x}\text{Mn}_x\text{As}$

A critical unresolved issue in the study of $\text{Ga}_{1-x}\text{Mn}_x\text{As}$ is the nature of the electronic structure in the heavily doped system. Spectroscopic data presented in the previous section clearly show that Mn-induced changes in the intragap response of $\text{Ga}_{1-x}\text{Mn}_x\text{As}$ are not merely restricted to the generation of charge carriers. Intriguingly, as much as 1.7% of Mn *does not* initiate any noticeable enhancement of the conductivity in the far-ir region, thus giving no indication for the presence of mobile holes. Hence this sample appears to be completely compensated. Since ferromagnetism in $\text{Ga}_{1-x}\text{Mn}_x\text{As}$ is believed to be mediated by conducting holes, compensation effects are likely to play a major role in defining not only electronic but also the magnetic state of a the doped system and therefore deserve careful consider-

ation. Although holes “neutralized” through the compensation processes do not participate in either dc or low- ω conductivity, these “neutral” states do contribute to optical absorption at higher energies. In order to illustrate a spectroscopic probe of compensation in a heavily doped system let us consider first the electronic structure of LT GaAs. The As_{Ga} defects form double donor levels 0.52 eV and 0.75 eV above the valence band.⁴¹ The concentration of these defects can be as high as 10^{20} cm^{-3} in LT GaAs films grown at 260–270°C. Tunnelling spectroscopy measurements for such samples have shown that these levels broaden to form a midgap deep donor band centered $\approx 0.5 \text{ eV}$ above the valence band.^{42,43} Transitions from the donor band to the conduction band (panel A Fig. 7) lead to a significant smearing of the fundamental absorption edge. As shown in Fig. 2 the optical conductivity of an LT GaAs sample grown under similar conditions to all $\text{Ga}_{1-x}\text{Mn}_x\text{As}$ studied in this work reveals characteristic “band-tailing” absorption with a sharp onset of $\sigma_1(\omega)$ at 7000 cm^{-1} (0.87 eV). This is consistent with earlier published results.^{35,36,44}

When Mn is substitutionally introduced in the GaAs host it is known to form a shallow acceptor level approximately 0.11 eV above the valence band. The presence of such an acceptor level has been verified by optical absorption studies.^{4,5} In LT GaAs samples doped with Mn we would expect an additional absorption structure directly attributable to compensation. Indeed, in Mn-doped samples the As_{Ga} antisite levels become depopulated and therefore can serve as final states for transitions from both the valence band and Mn-induced levels. Similar absorption is likely to occur in all *p*-doped LT GaAs samples. As illustrated in panel B of Fig. 7, the energy position of As_{Ga} levels and Mn acceptor levels is such that the onset of band tailing in a (partially) compensated sample is expected to shift to approximately 0.4 eV. This scenario is fully consistent with our data for the $x=0.017$ sample where a noticeable shift is revealed in the band tail to frequencies as low as 2500 cm^{-1} (0.31 eV). Depopulation of As_{Ga} levels also neutralizes holes produced by Mn doping (or any other form of *p* doping). In the absence of the As_{Ga} antisite band 1.7% of Mn in GaAs is expected to induce strong Drude-like absorption in the far-ir region with a plasma frequency $\omega_{pD} = 4\pi n e^2 / m^* = 5800 \text{ cm}^{-1}$ (assuming free electron mass). A primary impact of compensation is that the spectral weight is removed from the Drude channel to be recovered in the band-tail absorption. Integrating the area under the band tail in the $x=1.7\%$ film we obtained the plasma frequency of 3700 cm^{-1} . This value is somewhat lower than our estimate for $\omega_{p,D}$. This discrepancy is expected because interband absorption involving neutralized holes is likely to extend beyond the transmission cutoff imposed by the GaAs substrate, and therefore beyond the reach of our current data set.

For the series of $\text{Ga}_{1-x}\text{Mn}_x\text{As}$ samples studied here a Mn concentration of $x \approx 0.017$ appears to correspond to a critical level of compensation when all holes are neutralized by As_{Ga} states. At higher densities of Mn, free carrier absorption is evident in the data. The conjecture that the compensating capacity of antisite defects has been exhausted for $x > 0.017$ is supported by insensitivity of the band-tailing ab-

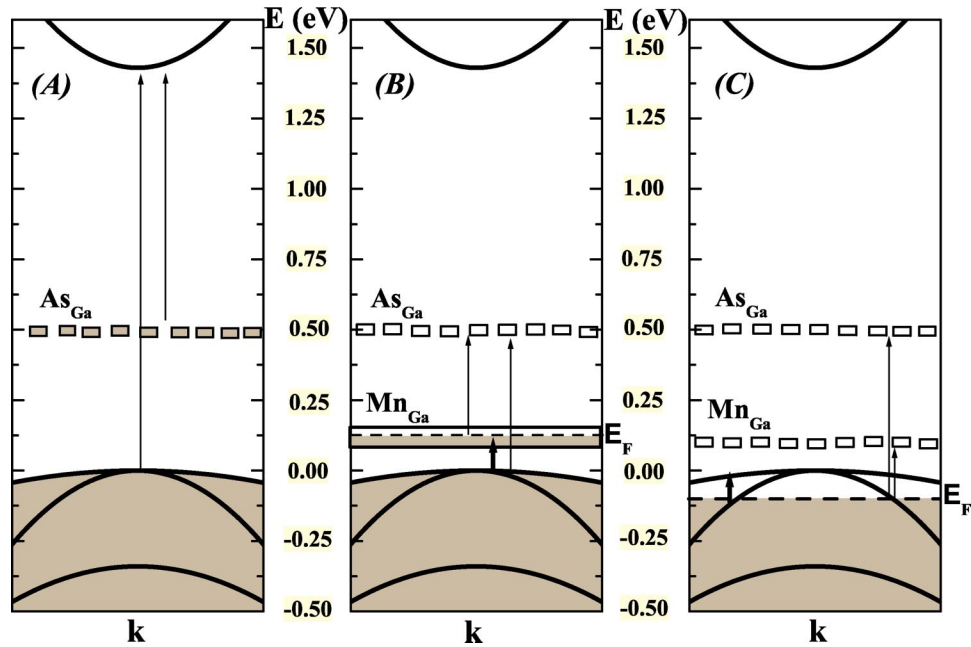


FIG. 7. Panel A shows the electronic structure of LT GaAs. According to tunneling spectroscopic measurements As_{Ga} levels in LT GaAs broaden to form bound centers approximately 0.5 eV above the valence band. The presence of As_{Ga} antisites causes the significant band-tailing observed in Fig. 2. Panels B and C show two possible scenarios for the evolution of the GaAs band structure with heavy Mn doping. Optical transitions corresponding to band-tailing effects are shown with thin arrows. The thick arrows indicate possible transitions which may be responsible for the low energy resonance observed in $\sigma_1(\omega)$. In panel B an impurity band is formed at the energy of the Mn acceptor level. If this band is partially occupied, metallic transport can occur and optical transitions are allowed originating from the valence band. Additionally the increase in band tailing as observed in Fig. 2 is expected when the As_{Ga} sites become depopulated. Panel C shows an alternative scenario where holes are doped into the valence band from Mn acceptor levels. Inter-valence band transitions can now occur, in addition to the band-tailing effects discussed previously.

sorption to the doping level beyond 1.7%. Nevertheless, data plotted in Fig. 3 are indicative of additional compensation channels unrelated to antisites. Indeed, the spectral weight [Eq. (1)] in the intragap conductivity first increases with the increase of Mn concentration but decreases for $x > 5.2\%$. This *nonmonotonic* dependence of the spectral weight on x points to the fact that Mn dopants not only act as acceptors in the GaAs host but also produce donor states. The latter role is expected if Mn enters the GaAs host interstitially.^{45–47} The doping dependence of the electronic spectral weight discussed above suggests that the fraction of Mn occupying interstitial sites is enhanced at $x > 5.2\%$. One aspect of Mn self-compensation which is not entirely clear is the precise location of the spectral weight associated with the transitions to Mn-induced donor levels. Density functional theory results by Erwin and Petukhov⁴⁵ predict that the relevant energy levels are likely to occur at energies close to 0.7 eV and 0.9 eV above the valence band. This position of the energy levels implies that a depression of the far-ir conductivity attributable to partial neutralization of mobile holes has to be accompanied with the increase of absorption at frequencies at $\omega > 0.7$ eV. Such an increase is not evident in our data. We therefore speculate that the levels associated with Mn interstitial are likely to occur much closer to the bottom of the conduction band. Accurate measurements of the optical constants as a function of doping and temperature at energies above the fundamental absorption edge are needed to resolve this issue.

B. Electronic structure of ferromagnetic $Ga_{1-x}Mn_xAs$

When constructing theories of carrier mediated ferromagnetism, identifying the band in which the itinerant carriers reside is of fundamental importance. This issue has led to lively discussion in the literature over the last several years. According to one school of thought, the doped carriers are assumed to reside in an impurity band (IB).^{6,9,20,21,28,48,49} This picture stems from the fact that Mn is known to form a shallow acceptor level in GaAs when the doping is weak (10^{17} cm^{-3}).^{4,5} The impurity band scenario assumes that as doping progresses from this very dilute limit, to the heavily doped regime, the shallow Mn acceptor level broadens and forms an impurity band (panel B in Fig. 7). An alternative scenario suggests that holes are doped into the GaAs valence band (VB).^{3,22–24,50} Within these models, the role of Mn doping is primarily restricted to increase of the hole concentration (panel C in Fig. 7). In the following we will test the validity of these proposals based on the current experimental results.

A key feature of the data presented earlier is the strong midinfrared absorption, observed exclusively in ferromagnetic samples. This feature has a natural explanation within the impurity band picture of the electronic structure. Returning to Fig. 3, $\sigma_1(\omega)$ is also shown for a very dilute sample of $Ga_{1-x}Mn_xAs$ with a Mn content of $x \sim 0.00002$.⁴ Below 800 cm^{-1} , $\sigma_1(\omega)$ is zero in the dilute Mn sample, as in the undoped GaAs. However, at higher energies an absorption

band is observed. This absorption is attributed to electronic transitions from the valence band to the Mn impurity level, which from this data lies about 800 cm^{-1} above the top of the valence band. Examining the data for the ferromagnetic films in Fig. 3 we see a strong correspondence between the position of the Mn impurity level in the dilute limit, and the strong absorption observed in the ferromagnetic system.⁵¹ While at this doping levels it is unlikely that an isolated Mn impurity level remains, the data of Fig. 2 suggest that transitions from the valence band to Mn-related electronic states may be the origin of the strong infrared absorption.

Alternatively, the midinfrared absorption may be accounted for without invoking an impurity band model. Internal structure of the valence band in III-V materials may give rise to a variety of absorption processes provided the system is heavily doped.⁵² Specifically, if E_F is located as depicted in panel C of Fig. 7, transitions are available between the heavy hole, light hole, and split off bands. The expected energy and oscillator strength of the transitions, which depend on the subband masses, spin-orbit energy, and doping level, are consistent with the resonance we observe near 2000 cm^{-1} .^{23,24}

While both models can explain the absorption band in the midinfrared, critical differences can be found in the predicted band structure properties. Specifically, the itinerant carrier mass will be significantly heavier in the impurity band than the GaAs valence band. The mass of the charge carriers may be accessed through a sum rule analysis of the intraband response in $\sigma_1(\omega)$ [Eq. (1)] provided that the carrier density is known. In practice an accurate determination of m^* is complicated by the compensation effects discussed earlier, and an accurate deconvolution of the intraband and interband contributions of $\sigma_1(\omega)$. Nevertheless, examination of the phase space of realistic values of m^* provides useful insight into the origin of the itinerant carriers. Following the procedure outlined in Ref. 26 we separate the intra- and interband components of the conductivity spectra in Fig. 3. We first assume no compensation and thus assign one charge carrier for every Mn atom in $\text{Ga}_{1-x}\text{Mn}_x\text{As}$. For the $x=0.052$ sample, which has the greatest spectral weight, integration of the intraband components yields values of the effective mass between $m^*=(2.1-44)m_e$. A direct integration of the entire $\sigma_1^m(\omega)$ spectrum also yields a mass of $m^*=2.1m_e$.²⁶ The above estimates are considerably reduced if compensation effects are considered. Discussion in the Sec. IV A clearly illustrates that as much as 1.7% of Mn does not deliver any mobile holes suggesting at least a 30% compensation level in the $x=0.052$ film. High field Hall measurements support this conclusion where the hole doping was found to be only one third of the Mn concentration.⁵³ Taking into account these results our estimates of the mass are reduced to $(0.7-15)m_e$. Table I summarizes the range of possible masses for all the different ferromagnetic samples, with the effects of compensation included.

These estimates are consistent with ARPES results¹⁵ which find a flat impurity band at the Fermi level, but exceed theoretical estimates of the mass of a 5% sample in a model where the holes are doped into the GaAs valence band and produce $m_B=0.25m_e$.²⁴ At this high doping level the nonpa-

rabolic character of the valence band may be partially responsible for this discrepancy. The effects of hybridization between the Mn acceptor levels and As p levels that make up the valence band can also lead to an enhanced mass. Indeed, the present experiments demonstrate the need to go beyond a simple picture of holes doped into unaltered GaAs bands. Additionally, mass enhancement may not solely a band structure effect, but caused by renormalization due to both lattice and magnetic polarons.³¹ Indeed, in this context it is worthwhile to mention that the sum rule analysis yields effective mass m^* which may significantly exceed the band mass m_b . It is the m_b value that is relevant to attempts to discriminate between the impurity band and valence band pictures of the electronic structure. Consideration of possible role of polaronic effects is the obvious next step in understanding these materials.

C. Hole dynamics in the ferromagnetic state

Having discussed the gross features of the electronic structure for $T>T_C$, we now explore the changes that occur at lower temperatures and how they are related to the onset of ferromagnetism. In Figs. 4 and 5 a nonmonotonic temperature dependence was observed in the low-energy part of the $\sigma_1(\omega)$ spectra. As the bottom panel of Fig. 5 demonstrates, this is due to a growth of low- ω spectral weight below T_C . In order to quantify this effect we calculate the intraband spectral weight using Eq. (1). In Fig. 8 we plot the differential spectral weight defined as $\delta(n/m^*)=(n/m^*)_T - (n/m^*)_{T_C}$ for all ferromagnetic samples. For this calculation the upper bound of the intraband spectral weight was used. For the $x=0.052$ sample, we also show the temperature dependence of $\delta(n/m^*)$ using the lower bound estimate of the intraband spectral weight and also for just integrating the entire $\sigma_1(\omega)$ curve to 4000 cm^{-1} at each temperature (see Ref. 26). Regardless of the method employed the principal trends are the same. Below T_C , $\delta(n/m^*)$ begins to increase, and continues to grow until the lowest temperature studied. This behavior is seen for all Mn-doping levels.

Also plotted in Fig. 8 is the magnetization of the samples. The strong correlation between the temperature dependence of the low- ω spectral weight and magnetization indicates that the heavy itinerant carriers may be mediating the ferromagnetism. Changes in the carriers effective mass below T_C have also been observed in the manganites⁵⁴⁻⁵⁶ and hexaborides,⁵⁷ both itinerant ferromagnets. A theory of kinetic energy driven ferromagnetism proposed by Hirsch⁵⁸ can account for this behavior. In the top left panel of Fig. 8 the relation between spectral weight and the gross magnetic properties of $\text{Ga}_{1-x}\text{Mn}_x\text{As}$ is further quantified. While the data for individual samples is rather sparse, the overall trend of several Mn dopings indicates a linear scaling between changes in the spectral weight and the square of the magnetization. This form of scaling relation is also observed in the manganites^{54,55} and can be accounted for within the double exchange model.⁵⁹

The data in Fig. 8 indicate that the changes in low- ω spectral weight has its origin in magnetic interactions. With this in mind we can get an estimate of the relevant energy

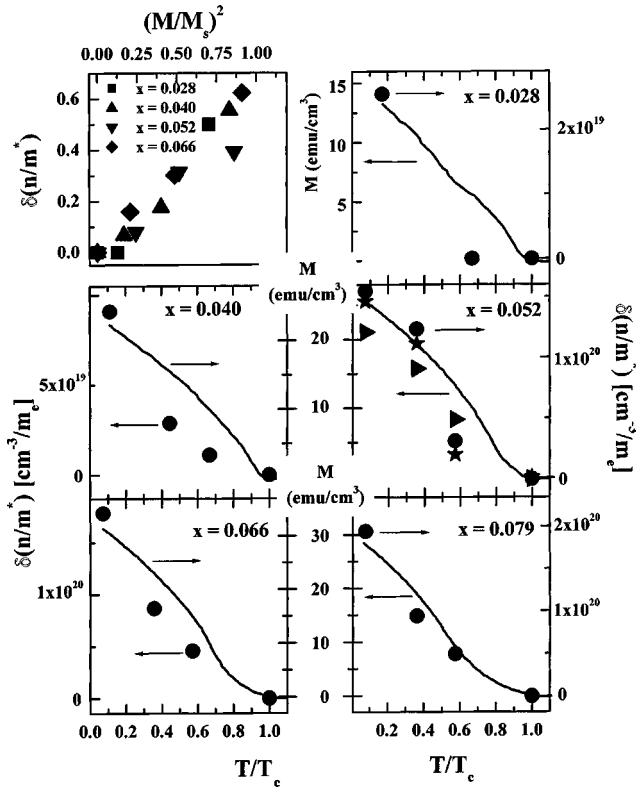


FIG. 8. Change in the spectral weight below T_C , $\delta(n/m^*) = (n/m^*)_T - (n/m^*)_{T_C}$, of the intraband component of $\sigma_1(\omega)$ calculated for all samples using the maximum spectral weight. For all samples a strong increase is observed below T_C . For the $x = 0.052$ sample $\delta(n/m^*)$ was also calculated with the minimum spectral weight (stars $\times 25$), and from a direct integration of $\sigma_1(\omega)$ up to 4000 cm^{-1} (triangles $\times 125$) (Ref. 26). All methods give the same qualitative result. Also plotted is the magnetization for each sample. The top left panel shows $\delta(n/m^*)$ normalized to the magnitude of the spectral weight at T_C plotted against the square of the magnetization. All samples show the same scaling regardless of T_C or Mn doping.

scales by looking at the frequency dependence of the spectral weight above and below T_C . To this end it is useful to compare the partial sum rule of Eq. (1), which defines the spectral weight, to the global sum rule

$$\frac{n}{m_e} = \frac{2}{\pi e^2} \int_0^\infty \sigma_1(\omega) d\omega, \quad (2)$$

which simply states that the total area under the conductivity curve is a constant, independent of external parameters such as temperature. Equation (2) demands that at some cutoff frequency $\Omega = \Omega_C$ the partial sum rule of Eq. (1) will become temperature independent. In Fig. 9 we plot the spectral weight [Eq. (1)] as a function of cut-off frequency Ω at $T = T_C$ and 5 K. For all the samples the spectral weight in the ferromagnetic state is enhanced at low energies. However, by $\Omega \leq 8000 \text{ cm}^{-1}$ the relative difference in spectral weight is less than 5% for the different temperatures ($\Omega = \Omega_C$, see arrows). This means that the low- ω spectral weight gained in the ferromagnetic state originated from energies $\leq 8000 \text{ cm}^{-1}$ (1 eV). This provides a rough estimate of the energy scale of the magnetic interactions. Indeed, in the manganites the low-frequency spectral weight is drawn from an energy range of $\sim 3 \text{ eV}$, which is the energy scale of the Hunds exchange coupling relevant to the manganite system.^{54,56} In contrast the Mn ion in $\text{Ga}_{1-x}\text{Mn}_x\text{As}$ is in the d^5 state,^{5,60} so the Hunds coupling is not the relevant exchange interaction. Rather a smaller kinetic exchange should apply, consistent with the lower energy scale of the spectral weight convergence observed in Fig. 9. While Ω_C for all Mn dopings is in the general range of $4000\text{--}8000 \text{ cm}^{-1}$, a definite pattern in the doping dependence is observed. In the top left panel of Fig. 9 Ω_C is plotted as a function of Mn dopings. At low dopings Ω_C increases linearly and then saturates at higher Mn concentration. Interestingly the doping dependence of Ω_C shows a remarkable similarity to the doping dependence of T_C shown in the inset of Fig. 3.

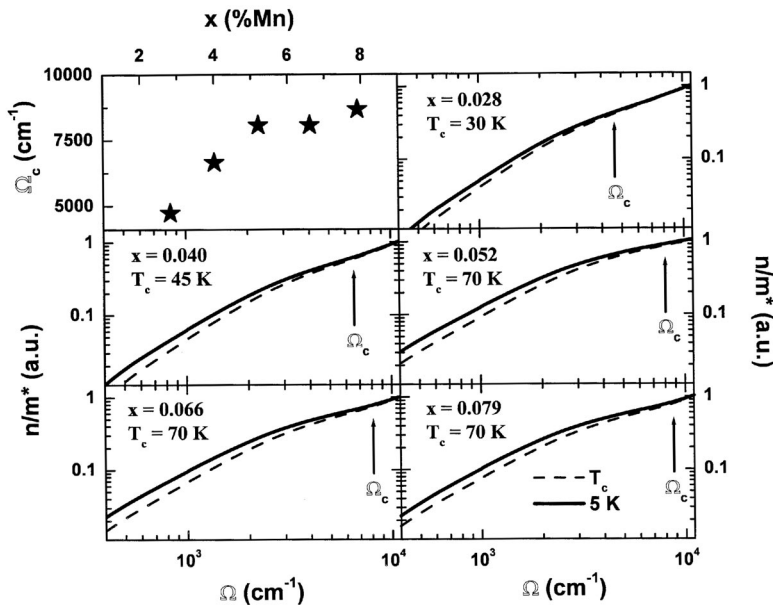


FIG. 9. Frequency dependence of the spectral weight [Eq. (1)] for all ferromagnetic samples at $T = T_C$ and 5 K. Throughout most of the frequency range there is more spectral weight in the ferromagnetic state. However, by $4000\text{--}8000 \text{ cm}^{-1}$ data at all temperatures converge to the same value. The arrows mark Ω_C , defined as the energy at which there is less than 5% relative differences in the spectral weight above and below T_C . The top left panel shows the doping dependence of Ω_C , which has a striking resemblance to the doping dependence of T_C (inset of Fig. 3).

V. SUMMARY AND OUTLOOK

In this work we have employed a novel approximation free method for extracting the optical constants of a 2 layer system to investigate the electronic structure and dynamic properties of $\text{Ga}_{1-x}\text{Mn}_x\text{As}$. We have expanded on our earlier work by further examining trends in the evolution of $\sigma_1(\omega)$ throughout the magnetic phase diagram. Using optical sum rules we have performed a model independent analysis to explore both the effects of compensation at different dopings and changes in the effective mass of the itinerant carriers at $T < T_C$.

The main features of the electromagnetic response of $\text{Ga}_{1-x}\text{Mn}_x\text{As}$ include a broadening of the band edge seen in all samples, a resonance centered near 2000 cm^{-1} , and a Drude (free carrier) absorption at low energies; the latter two features are detected only in ferromagnetic films. The strong intragap absorption structure at 2000 cm^{-1} has been discussed in terms of both transitions to an impurity band and intervalence transitions. While both ideas can reproduce the energy scale of the absorption resonance, neither can completely account for all of the data. In particular, sum rule analysis of the infrared conductivity suggests that the effective mass of the itinerant carriers is $(0.7-15)m_e$. A realistic picture of the electronic structure has to include hybridization effects between the Mn-induced impurity band and the valence band of the GaAs host.

Sum rules were also utilized to examine temperature dependent changes in the Drude contribution to $\sigma_1(\omega)$. In particular, we observe a strong enhancement of low-energy spectral weight below the ferromagnetic transition. This enhancement is understood in terms of a decrease in the carrier mass in the ferromagnetic state. The change in spectral weight is found to scale with the magnetization for all Mn dopings studied. The spectral weight becomes temperature independent near 8000 cm^{-1} , which supports a small exchange coupling in this system. The doping dependence of the spectral weight was also examined and correlated well with T_C , further supporting a picture of ferromagnetism mediated by heavy conducting holes. We emphasize that the effective mass inferred from the analysis of the spectroscopic data may be enhanced compared to the band mass due to many-body effects. These effects are outside the scope of the present paper but deserve further examination.

We have presented a detailed discussion of compensation effects in $\text{Ga}_{1-x}\text{Mn}_x\text{As}$ based on the analysis of the frequency dependence of the conductivity. We have shown that in fully compensated samples the role of Mn doping is restricted to broadening of the fundamental absorption edge. The gap edge structure is reminisced of that of LT GaAs but is shifted to lower energies in quantitative agreement with the energetics of As_{Ga} antisite levels and Mn-induced levels in the GaAs host. We can estimate a low bound of the compensation level due to As_{Ga} antisites in $\text{Ga}_{1-x}\text{Mn}_x\text{As}$, which is about 30%. Another form of compensating defects is found in heavily doped samples ($x > 5\%$) and is attributed to Mn interstitials. The nonmonotonic dependence of the intragap spectral weight with doping detected in our measurements indicates that the enhancement of T_C cannot be readily

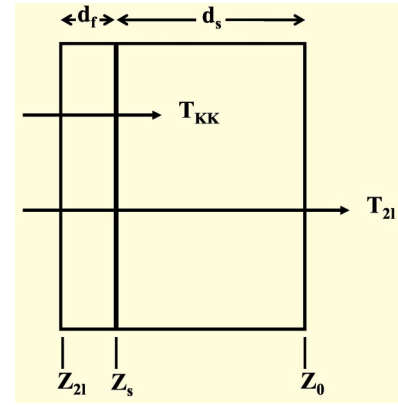


FIG. 10. Representation of the experimental geometry. The measured quantity is T_{2l}/T_{sub} , where T_{sub} is the transmitted intensity through a blank substrate. The desired quantity for Kramers-Kronig analysis is the transmission through the film into the substrate (T_{KK}), which can be obtained from the experimental data and substrate properties from Eq. (A11) as explained in the text. Z_{2l} , Z_s , and Z_0 correspond to the load at each interface.

achieved by trivial increase of Mn concentration since $\text{Ga}_{1-x}\text{Mn}_x\text{As}$ is a strongly compensated system. Recent transport and magnetic measurements have indicated that proper heat treatment of $\text{Ga}_{1-x}\text{Mn}_x\text{As}$ films during and/or after the growth can dramatically enhance the Curie temperature.^{61,62} This enhancement has been attributed to a reduction of defects in the material; however, to date this has not been verified experimentally. It will be instructive to explore this behavior in the context of redistribution of the electronic spectral weight. In particular the changes in a number of parameters (i.e., effective mass, scattering rate, etc.) may be deduced, giving further insight into the dynamics of these materials.

ACKNOWLEDGMENTS

This work was supported by the DOE, NSF, DARPA, and ONR. We would like to thank P. Henning for his help with the impedance theory. We would like to acknowledge numerous discussions with C. Cuiti, A. MacDonald, L.J. Sham, and J. Sinova.

APPENDIX

1. Kramers-Kronig analysis of a two-layer system

Obtaining the optical constants from transmission measurements is complicated by the fact that the film of interest is deposited on a substrate. The experimentally accessible quantity is the transmission through the film/substrate two layer system, T_{2l} (Fig. 10). This transmission will depend on six parameters: the real and imaginary parts of both the film and substrate optical constants, and the thickness of both the film and substrate. In general both thicknesses, and the optical constants of the substrate are known *a priori*, leaving two unknown quantities: the real and imaginary optical constants of the film. However, knowledge of the transmission of the two layer system alone is insufficient in determining these parameters.

A second piece of information is required in order to uniquely solve for the optical constants. One approach is to additionally measure the near normal incidence reflectance of the film/substrate system (R_{2l}). The two unknown quantities can then be determined from R_{2l} and T_{2l} .⁶³ An alternative method employed here is to make use of the KK relations in order to calculate the phase change of the transmitted light. With the transmission and phase we can then calculate the optical constants of the film. As will be discussed later we do measure R_{2l} in the mid infrared at 292 K and calculate the optical constants directly, in order to set a constraint on our KK analysis.

In the analysis of reflectance measurements, the Kramers-Kronig relations are routinely used to generate the phase corresponding to the measured reflectance. With this information the optical constants are then calculated. Using this method for transmission experiments introduces additional complications as well as the known problem of integration limits encountered in reflectance measurements. The transmission, T , of a single layer determines the amplitude of the complex transmission coefficient: $\hat{t} = \sqrt{T}e^{i\theta}$. The KK integral relating the measured amplitude to the unknown phase of a electromagnetic wave passing through a *single layer* is⁶⁴

$$\theta(\omega_0) = -(2\omega_0/\pi) \int_0^\infty \frac{\ln[|\hat{t}(\omega)|/|\hat{t}(\omega_0)|]}{\omega^2 - \omega_0^2} d\omega + 2\pi\omega_0 d_f, \quad (\text{A1})$$

where d_f is the thickness of the film. It is worth emphasizing that Eq. (A1) only applies to a single free-standing layer. We are not aware of a corresponding equation for a two layer system. The main challenge in applying the KK approach to transmission measurements is to deconvolve the measured T_{2l} into an effective one-layer transmission. Often this is done through an iterative process where by first guessing values of the films optical constants the transmission through the film and substrate can be easily separated allowing for a KK analysis of the films transmission yielding a new set of optical constants for the film. This processes is repeated until the values of the films optical constants converge.^{63,65}

In the present analysis we use an alternative technique which is free of approximations, and does not require numerous iterations.³⁰ Using the formalism of impedance theory⁶⁶ the transmission across any boundary can be written in terms of the intrinsic impedance $\eta(\omega) = 120\pi/\hat{n}(\omega)$ and propagation constant $\gamma(\omega) = 2\pi\omega\hat{n}(\omega)$ of the material [$\hat{n}(\omega)$ is the complex index of refraction], and the load at the boundary, Z (Fig. 10). The load at the vacuum-film interface is given by

$$Z_{2l} = \eta_f \frac{Z_s \cosh(\gamma_f d_f) + \eta_f \sinh(\gamma_f d_f)}{\eta_f \cosh(\gamma_f d_f) + Z_s \sinh(\gamma_f d_f)}, \quad (\text{A2})$$

while the load at the film-substrate interface is

$$Z_s = \eta_s \frac{Z_0 \cosh(\gamma_s d_s) + \eta_s \sinh(\gamma_s d_s)}{\eta_s \cosh(\gamma_s d_s) + Z_0 \sinh(\gamma_s d_s)}, \quad (\text{A3})$$

where the subscript f labels the properties of the film and the subscript s corresponds to the substrate. $Z_0 = 377 \Omega$ is the

impedance of free space. The complex transmission coefficient for the two layer system is given by

$$\hat{t}_{2l} = \frac{\eta_f + Z_{2l}}{Z_0 + Z_{2l}} \frac{\eta_s + Z_s}{\eta_f + Z_s} \frac{2Z_0}{\eta_s + Z_0} e^{-(d_f \gamma_f + d_s \gamma_s)}. \quad (\text{A4})$$

Additionally, the complex reflectivity for the thin film side is

$$\hat{r}_{2l} = \frac{Z_{2l} - Z_0}{Z_{2l} + Z_0}. \quad (\text{A5})$$

The problem now is to deconvolve the two layer transmission ($T_{2l} = \hat{t}_{2l}^* \hat{t}_{2l}$) into an equivalent one layer transmission. For this purpose it is instructive to first consider the slightly different geometry of a single layer bounded on one side by vacuum and the other by an infinite substrate (Fig. 10 with $d_s \rightarrow \infty$). In this case we have

$$\hat{t}_{1l} = \frac{\eta_f + Z_{1l}}{Z_0 + Z_{1l}} \frac{2\eta_s}{\eta_f + \eta_s} e^{-d_f \gamma_f}, \quad (\text{A6})$$

where

$$Z_{1l} = \eta_f \frac{\eta_s \cosh(\gamma_f d_f) + \eta_f \sinh(\gamma_f d_f)}{\eta_f \cosh(\gamma_f d_f) + \eta_f \sinh(\gamma_f d_f)}. \quad (\text{A7})$$

Guided by the form of the right-hand side in Eq. (A6) we can now rewrite Eq. (A4) as

$$\hat{t}_{2l} = \hat{t}_{\text{KK}} \hat{t}_{\text{corr}}, \quad (\text{A8})$$

where

$$\hat{t}_{\text{corr}} = \frac{2Z_0}{\eta_s + Z_0} e^{-d_s \gamma_s} \quad (\text{A9})$$

and

$$\hat{t}_{\text{KK}} = \frac{\eta_f + Z_{2l}}{Z_0 + Z_{2l}} \frac{\eta_s + Z_s}{\eta_f + Z_s} e^{-d_f \gamma_f}. \quad (\text{A10})$$

First notice that \hat{t}_{corr} only depends on the properties of the substrate and therefore is entirely known. Now \hat{t}_{KK} is analogous to Eq. (A6), but is now the transmission into a *finite* thickness substrate. This is the quantity that we KK transform in order to get the corresponding phase spectrum. Experimentally, we measure the transmission of the two layer system relative to a bare substrate, $T_{\text{meas}} = T_{2l}/T_s$. Therefore from the experimental data and knowledge of the substrate properties we calculate the KK input for Eq. (A1) as

$$|\hat{t}_{\text{KK}}| = \frac{\sqrt{T_{\text{meas}} T_s}}{|\hat{t}_{\text{corr}}|}. \quad (\text{A11})$$

2. Kramers-Kronig extrapolations and reflectivity constraints

Having established the applicability of the Kramers-Kronig procedure we now comment on the inherent limitations of this method. Examination of Eq. (A1) reveals that the phase at any frequency depends on the transmission from $\omega=0$ to $\omega \rightarrow \infty$. For regions outside of the measured fre-

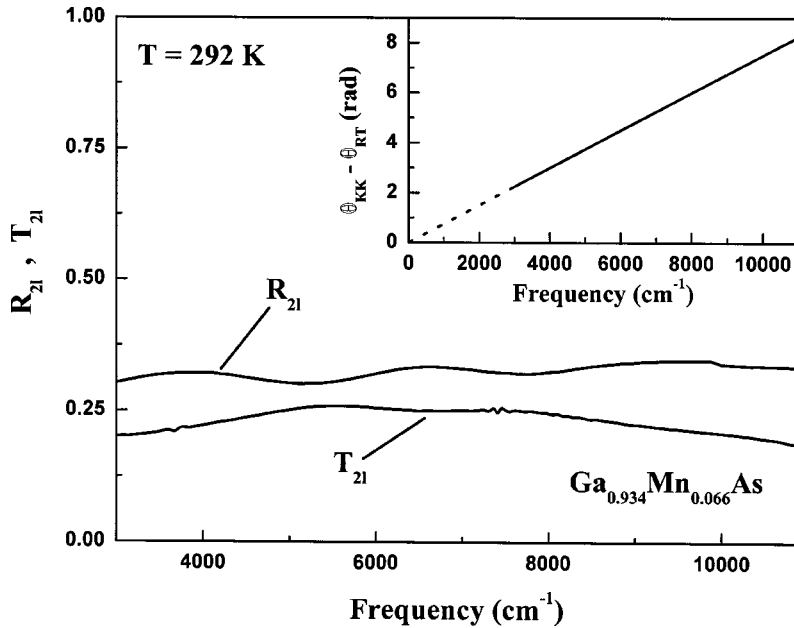


FIG. 11. Main panel shows R_{2l} and T_{2l} for the $x=0.066$ sample at $T=292$ K. These data are used to calculate $\sigma_1(\omega)$ shown in Fig. 12, and additionally obtain a phase correction factor for all ω and T of the $x=0.066$ sample. The inset shows the difference between the R_{2l} and T_{2l} phase and the KK phase obtained without a high- ω extrapolation (solid line). The observed linearity allows for a phase correction factor to be determined at all ω (dashed line).

frequency interval some value of the transmission must be assumed. For the current data set the low frequency extrapolation has a negligible impact on the optical constants in the measured bandwidth due to the low experimental cutoff (15 cm^{-1}). However, the present experimental configuration severely limits our high frequency cutoff due to the band gap in the GaAs substrate ($\sim 12000 \text{ cm}^{-1}$). Varying the high- ω extrapolation has a considerable impact on the KK-generated phase and therefore the final form of the optical constants. Thus, some method of constraining the phase is needed in order to obtain reliable results.

As discussed earlier, an alternative way of generating the optical constants without relying on the KK technique is to measure both T_{2l} and R_{2l} . Using Eqs. (A4) and (A5) the

optical constants of the film can be solved for directly. With this knowledge, Eq. (A10) can be used to calculate the correct phase directly, and therefore determine an appropriate correction factor for the KK phase. This procedure is illustrated in Figs. 11 and 12. The main panel of Fig. 11 shows the two layer reflectivity and transmissivity of the $x=0.066$ sample at 292 K. With this data Eqs. (A4) and (A5) were used to calculate $\sigma_1(\omega)$, shown with a thick line in Fig. 12. Also shown in Fig. 12 are two $\sigma_1(\omega)$ curves corresponding to the KK analysis of T_{2l} in Fig. 11 outlined in the previous section. In the first case the high- ω extrapolation used in Eq. (A1) to calculate the phase was $T_{KK}=0$. $\sigma_1(\omega)$ corresponding to this choice is shown with the dash-dotted line. There is a large suppression of $\sigma_1(\omega)$ relative to the T_{2l} and R_{2l}

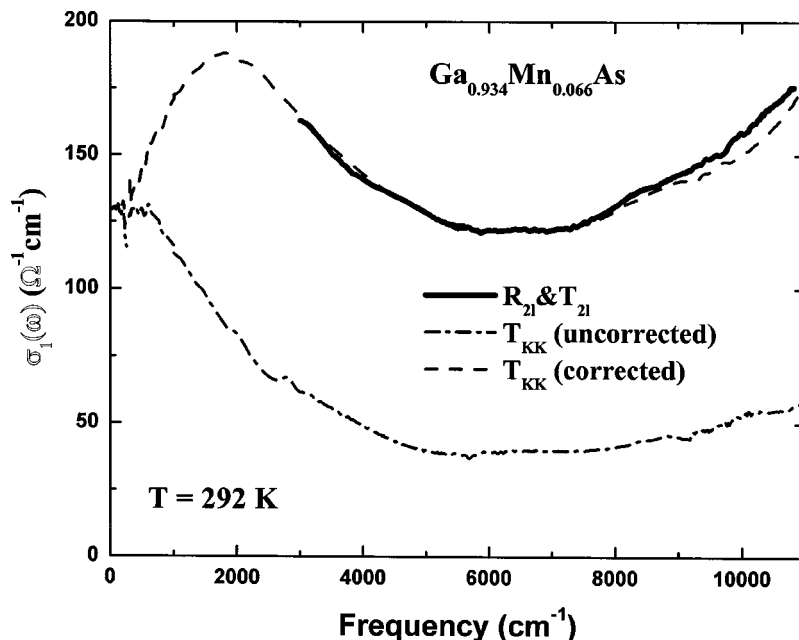


FIG. 12. $\sigma_1(\omega)$ for the $x=0.066$ sample at $T=292$ K obtained in various ways. The thick black line corresponds to a direct calculation from R_{2l} and T_{2l} shown in Fig. 11. The dot-dashed line was calculated from T_{2l} alone utilizing the KK relations without a high ω extrapolation. The strong discrepancies between these curves demonstrates the impact of using an incorrect extrapolation to calculate the phase. Finally, using the R_{2l} and T_{2l} results to correct the KK generated phase produces the dashed line, which is in full agreement with the direct R_{2l} and T_{2l} result.

method, and additionally, no finite frequency peak is observed, which as will be discussed below is a robust feature even in the raw data (Fig. 1).

The strong deviation between the two curves in Fig. 12 can be traced back to the incorrect KK generated phase due to the lack of high-frequency extrapolation. The error in the KK phase is illustrated in the inset of Fig. 11 where the difference between the KK-generated phase and the phase calculated from the results of the R_{2l} and T_{2l} measurements is plotted as a function of frequency (solid line). The fact that this difference is nearly linear is expected based on the form

of the KK equation,^{63,65} and provides a practical solution to finding the correct KK phase. Extrapolating the phase difference to low frequencies (dashed line) allows for a reliable determination of the phase even outside of the frequency interval where R_{2l} was measured. Additionally, the phase correction factor determined at 292 K can be used for all T , as evidenced by its lack of variation for samples with different Mn doping.⁶⁷ After the phase is corrected $\sigma_1(\omega)$ can again be calculated, and is shown in Fig. 12 as a dashed line. The agreement with the value directly obtained from the R_{2l} and T_{2l} data is excellent.

- *Present address: Advanced Light Source Division, Lawrence Berkeley National Laboratory, 1 Cyclotron Road, Berkeley, California 94720.
- †Present address: Department of Physics, University of California, Riverside, CA 92521.
- ¹H. Ohno, *Science* **281**, 251 (2001); H. Ohno, A. Shen, F. Matsukura, A. Oiwa, A. Endo, S. Katsumoto, and Y. Iye, *Appl. Phys. Lett.* **69**, 363 (1996).
- ²S.A. Wolf, D.D. Awschalom, R.A. Buhrman, J.M. Daughton, S. von Molnar, M.L. Roukes, A.Y. Chtchelkanova, and D.M. Treger, *Science* **294**, 1488 (2001).
- ³T. Dietl, H. Ohno, F. Matsukura, J. Cibert, and D. Ferrand, *Science* **287**, 1019 (2000); T. Dietl, *Semicond. Sci. Technol.* **17**, 377 (2002).
- ⁴R.A. Chapman and W.G. Hutchinson, *Phys. Rev. Lett.* **18**, 443 (1967).
- ⁵M. Linnarsson, E. Janzen, B. Monemar, M. Kleverman, and A. Thilderkvist, *Phys. Rev. B* **55**, 6938 (1997).
- ⁶H. Akai, *Phys. Rev. Lett.* **81**, 3002 (1998).
- ⁷M. Shirai, T. Ogawa, I. Kitagawa, and N. Suzuki, *J. Magn. Magn. Mater.* **177-181**, 1383 (1998).
- ⁸J.H. Park, S.K. Kwon, and B.I. Min, *Physica B* **281**, 703 (2000).
- ⁹J. Inoue, S. Nonoyama, and H. Itoh, *Phys. Rev. Lett.* **85**, 4610 (2000).
- ¹⁰S. Sanvito, P. Ordejon, and N.A. Hill, *Phys. Rev. B* **63**, 165206 (2001).
- ¹¹Yu-Jun Zhao, W.T. Geng, K.T. Park, and A.J. Freeman, *Phys. Rev. B* **64**, 035207 (2001).
- ¹²M. Jain, L. Kronik, J.R. Chelikowsky, and V.V. Godlevsky, *Phys. Rev. B* **64**, 245205 (2001).
- ¹³E. Kulatov, H. Nakayama, H. Mariette, H. Ohta, and Y.A. Uspenskii, *Phys. Rev. B* **66**, 045203 (2002).
- ¹⁴J. Okabayashi, A. Kimura, T. Mizokawa, A. Fujimori, T. Hayashi, and M. Tanaka, *Phys. Rev. B* **59**, 2486 (1999).
- ¹⁵J. Okabayashi, A. Kimura, O. Rader, T. Mizokawa, A. Fujimori, T. Hayashi, and M. Tanaka, *Phys. Rev. B* **64**, 125304 (2001).
- ¹⁶H. Ask Lund, L. Ilver, J. Kanski, J. Sadowski, and R. Mathieu, *Phys. Rev. B* **66**, 115319 (2002).
- ¹⁷G. Mahieu, P. Condet, B. Grandier, J.P. Nys, G. Allan, D. Stievenard, Ph. Ebert, H. Shimizu, and M. Tanaka, *Appl. Phys. Lett.* **82**, 712 (2002); T. Tsuruoka, N. Tachikawa, S. Ushioda, F. Matsukura, K. Takamura, and H. Ohno, *ibid.* **81**, 2800 (2002).
- ¹⁸S. Katsumoto, T. Hayashi, Y. Hashimoto, Y. Iye, Y. Ishiwata, M. Watanabe, R. Eguchi, T. Takeuchi, Y. Harada, S. Shin, and K. Hirakawa, *Mater. Sci. Eng., B* **84**, 88 (2001); K. Hirakawa, S. Katsumoto, T. Hayashi, Y. Hashimoto, and Y. Iye, *Phys. Rev. B* **65**, 193312 (2002).
- ¹⁹Y. Nagai, T. Kunimoto, K. Nagasaka, H. Nojiri, M. Motokawa, F. Matsukura, T. Dietl, and H. Ohno, *Jpn. Soc. Appl. Phys.* **11**, 6231 (2001).
- ²⁰M. Mayr, G. Alvarez, and E. Dagotto, *Phys. Rev. B* **65**, 241202 (2002); G. Alvarez, M. Mayr, and E. Dagotto, *Phys. Rev. Lett.* **89**, 277202 (2002); G. Alvarez and E. Dagotto, cond-mat/0303350 (unpublished).
- ²¹A. Chattopadhyay, S. Das Sarma, and A.J. Millis, *Phys. Rev. Lett.* **87**, 227202 (2001); E.H. Hwang, A.J. Millis, and S. Das Sarma, *Phys. Rev. B* **65**, 233206 (2002).
- ²²J. König, H.H. Lin, and A.H. MacDonald, *Phys. Rev. Lett.* **84**, 5628 (2000).
- ²³S.R. Eric Yang, Jairo Sinova, T. Jungwirth, Y.P. Shim, and A.H. MacDonald, *Phys. Rev. B* **67**, 045205 (2003).
- ²⁴J. Sinova, T. Jungwirth, S.R. Eric Yang, J. Kucera, and A.H. MacDonald, *Phys. Rev. B* **66**, 041202 (2002).
- ²⁵E. Shiles, T. Sasaki, M. Inokuti, and D.Y. Smith, *Phys. Rev. B* **22**, 1612 (1980).
- ²⁶E.J. Singley, R. Kawakami, D.D. Awschalom, and D.N. Basov, *Phys. Rev. Lett.* **89**, 097203 (2002).
- ²⁷S. Sanvito and N.A. Hill, *Appl. Phys. Lett.* **78**, 3493 (2001).
- ²⁸M. Berciu and R.N. Bhatt, *Phys. Rev. Lett.* **87**, 107203 (2001).
- ²⁹C. Timm, F. Schafer, and F. von Oppen, *Phys. Rev. Lett.* **89**, 137201 (2002).
- ³⁰P.F. Henning, E.J. Singley, D.N. Basov, C.C. Homes, and M. Strongin (unpublished).
- ³¹D.N. Basov, A.M. Bratkovsky, P.F. Henning, B. Zink, F. Hellman, Y.J. Wang, C.C. Homes, and M. Strongin, *Europhys. Lett.* **57**, 240 (2002).
- ³²The frequency resolution of T_{meas} was kept $\geq 4 \text{ cm}^{-1}$ in order to avoid resolving the interference due to the thick (0.5 mm) substrate. The frequency of these interference fringes were less than 0.5 cm^{-1} . Since we were unable to completely resolve this interference we used a much broader resolution to experimentally smoothen it out. This intrinsic smoothing was taken into account in our analysis.
- ³³E.D. Palik, *Handbook of Optical Constants of Solids* (Orlando, Academic Press, 1985).
- ³⁴While there is currently a body of work on LT GaAs, to the best of our knowledge the optical constants have not previously been reported, only the absorption coefficient.
- ³⁵M.O. Manasreh, D.C. Look, K.R. Evans, and C.E. Stutz, *Phys. Rev. B* **41**, 10272 (1990).
- ³⁶X. Liu, A. Prasad, W.M. Chen, A. Kurplewski, A. Stoschek, Z.

- Liliental-Weber, and E.R. Weber, *Appl. Phys. Lett.* **65**, 3002 (1994).
- ³⁷F. Matsukura, H. Ohno, A. Shen, and Y. Sugawara, *Phys. Rev. B* **57**, 2037 (1998).
- ³⁸M.J. Seong, S.H. Chun, H.M. Cheong, N. Samarth, and A. Mascarenhas, *Phys. Rev. B* **66**, 033202 (2002).
- ³⁹R. Moriya and H. Munekata, *Appl. Phys. Lett.* **93**, 4603 (2003).
- ⁴⁰K.M. Yu, W. Walukiewicz, T. Wojtowicz, W.L. Lim, X. Liu, Y. Sasaki, M. Dobrowolska, and J.K. Furdyna, *Appl. Phys. Lett.* **81**, 844 (2002).
- ⁴¹W.E. Spicer, P.W. Chye, P.R. Skeath, C.Y. Su, and I. Lindau, *J. Vac. Sci. Technol.* **16**, 1422 (1979); E.R. Weber, H. Ennen, V. Kaufmann, J. Windscheif, J. Schneider, and T. Wosinski, *J. Appl. Phys.* **53**, 6140 (1982).
- ⁴²R.M. Feenstra, A. Vaterlaus, J.M. Woodall, and G.D. Pettit, *Appl. Phys. Lett.* **63**, 2528 (1993).
- ⁴³S. Lodha, D.B. Janes, and N.P. Chen, *J. Appl. Phys.* **93**, 2772 (2003).
- ⁴⁴It should be noted that studies on semi-insulating GaAs have produced similar results due to the EL2 defect, a well known native defect in this material ($\sim 10^{16} \text{ cm}^{-3}$); however they are three orders of magnitude smaller than in LT GaAs. G.M. Martin, *Appl. Phys. Lett.* **39**, 747 (1981); P. Omling, E.R. Weber, and L. Samuelson, *Phys. Rev.* **33**, 5880 (1986).
- ⁴⁵S.C. Erwin and A.G. Petukhov, *Phys. Rev. Lett.* **89**, 227201 (2002).
- ⁴⁶F. Maca and J. Masek, *Phys. Rev. B* **65**, 235209 (2002).
- ⁴⁷K.M. Yu, T. Walukiewicz, T. Wojtowicz, I. Kuryliszyn, X. Liu, Y. Sasaki, and J.K. Furdyna, *Phys. Rev. B* **65**, 201303 (2002).
- ⁴⁸V.A. Ivanov, P.M. Krstajic, F.M. Peeters, V. Fleurov, and K. Kikoin, *J. Magn. Magn. Mater.* **258–259**, 237 (2003).
- ⁴⁹A. Kaminski and S. Das Sarma, *Phys. Rev. Lett.* **88**, 247202 (2002).
- ⁵⁰G. Zarand and B. Janko, *Phys. Rev. Lett.* **89**, 047201 (2002).
- ⁵¹For the data of the $x=0.017$ sample we cannot rule out a similar feature, which could be up to five times stronger than the data for the dilute nonmagnetic crystal.
- ⁵²R. Braunstein and E.O. Kane, *J. Phys. Chem. Solids* **23**, 1423 (1962).
- ⁵³H. Ohno, F. Matsukura, T. Omiya, and N. Akiba, *J. Appl. Phys.* **85**, 4277 (1999).
- ⁵⁴Y. Okimoto, T. Katsufuji, T. Ishikawa, T. Arima, and Y. Tokura, *Phys. Rev. B* **55**, 4206 (1997).
- ⁵⁵K.H. Kim, J.H. Jung, D.J. Eom, T.W. Noh, J. Yu, and E.J. Choi, *Phys. Rev. Lett.* **81**, 4983 (1998).
- ⁵⁶M. Quijada, J. Cerne, J.R. Simpson, H.D. Drew, K.H. Ahn, A.J. Millis, R. Shreekala, R. Ramesh, M. Rajeswari, and T. Venkatesan, *Phys. Rev. B* **58**, 16093 (1998).
- ⁵⁷S. Broderick, B. Ruzicka, L. Degiorgi, H.R. Ott, J.L. Sarrao, and Z. Fisk, *Phys. Rev. B* **65**, 121102 (2002).
- ⁵⁸J.E. Hirsch, *Phys. Rev. B* **62**, 14131 (2000).
- ⁵⁹N. Furukawa, *J. Phys. Soc. Jpn.* **63**, 3214 (1994).
- ⁶⁰J. Schneider, U. Kaufmann, W. Wilkening, M. Baeumler, and F. Kohl, *Phys. Rev. Lett.* **59**, 240 (1987).
- ⁶¹S.J. Potashnik, K.C. Ku, S.H. Chun, J.J. Berry, N. Samarth, and P. Schiffer, *Appl. Phys. Lett.* **79**, 1495 (2001).
- ⁶²K.W. Edmonds, K.Y. Wang, R.P. Champion, A.C. Neumann, N.R.S. Farley, B.L. Gallagher, and C.T. Foxon, *Appl. Phys. Lett.* **81**, 4991 (2002).
- ⁶³P.O. Nilsson, *Appl. Opt.* **7**, 435 (1968).
- ⁶⁴S. Maeda, G. Thyagarajan, and P.N. Shatz, *J. Chem. Phys.* **39**, 3474 (1963).
- ⁶⁵J.D. Neufeld and G. Andermann, *J. Opt. Soc. Am.* **62**, 1156 (1972).
- ⁶⁶S. Rammo and J.R. Whinnery, *Fields and Waves in Modern Radio* (Wiley, New York, 1953).
- ⁶⁷The phase correction factor (slope of line in inset of Fig. 11) changed by 4% from the most transparent sample ($x=0.017$) to the most opaque sample ($x=0.052$). As illustrated in Fig. 1 the changes in the transmission spectrum between these samples far exceeds the changes induced with changing temperature for any one sample. Varying the phase correction factor by 4% for a given sample and temperature has a negligible effect on $\sigma_1(\omega)$. Thus, determining the phase correction factor at only one temperature does not introduce any noticeable errors into the analysis.